RSC Advances

PAPER

View Article Online
View Journal | View Issue

Cite this: *RSC Adv.*, 2026, **16**, 5652

Rational design and synthesis of new acetamide–indole–benzo[*d*]imidazole–carboxylic acid hybrids as dual PTP1B/α-glucosidase inhibitors

Navid Dastyafteh,[a] Seyedeh Niloufar Ghafouri,[b] Marjan Mollazadeh,[c] Nazanin Motamedi Shakib,[b] Mohammad Halimi,[d] Samanesadat Hosseini,[e] Somayeh Mojtabavi,[f] Mohammad Ali Faramarzi,[f] Bagher Larijani,[c] Massoud Amanlou,[g] Maryam Mohammadi-Khanaposhtani *[h] and Mohammad Mahdavi *[c]

A series of novel acetamide–indole–benzo[*d*]imidazole–carboxylic acid hybrids (**8a–n**) was designed based on the structural scaffolds of known protein tyrosine phosphatase 1B (PTP1B) and α-glucosidase inhibitors. Evaluation against PTP1B revealed that six compounds (**8d**, **8f–h**, **8j**, and **8l**) exhibited superior inhibitory activity compared to the standard inhibitor suramin, while one derivative (**8a**) demonstrated comparable potency. The remaining compounds showed reduced efficacy relative to suramin. In contrast, only two compounds (**8j** and **8k**) displayed marginally superior α-glucosidase inhibition compared to acarbose, while all other derivatives were less potent than the standard. Based on these results, subsequent investigations focused on the PTP1B inhibitory potential of this series. Kinetic analysis of the most potent compound, **8l**, confirmed a competitive inhibition mechanism against PTP1B. Molecular docking studies of the most active compounds yielded binding modes consistent with the *in vitro* activity, and molecular dynamics simulations further verified the stable binding of compound **8l** within the PTP1B active site, supporting its potential as a lead PTP1B inhibitor.

Received 16th October 2025
Accepted 2nd January 2026

DOI: 10.1039/d5ra07935g

rsc.li/rsc-advances

Introduction

Diabetes mellitus, specifically type 2, and obesity are two important metabolic disorders that require multi-target therapeutic strategies for effective management.[1,2] Two important targets for treating these disorders are protein tyrosine phosphatase 1B (PTP1B) and α-glucosidase.[3] PTP1B is primarily a hepatic enzyme that negatively regulates both insulin and leptin signaling, and α-glucosidase is an intestinal enzyme for digestive carbohydrates.[4,5] The inhibition of PTP1B enhances systemic insulin sensitivity and modulates energy balance, while α-glucosidase inhibition locally reduces glucose absorption.[6,7]

Multi-target drug design is a valuable goal in modern medicinal chemistry for the treatment of complex disorders like diabetes and obesity.[8] The multifaceted pathogenesis of these metabolic diseases provides a strong rationale for developing multi-target ligands to overcome the limitations of conventional single-target therapies.[9] In this regard, the design of lead compounds targeting both PTP1B and α-glucosidase is a valuable pursuit for medicinal chemists.[3] In this endeavor, the molecular hybridization of effective pharmacophores presents a particularly powerful and beneficial strategy.[10]

Based on this rationale, we initiated an investigation into novel compounds with the objective of developing dual-target inhibitors capable of simultaneously modulating both PTP1B and α-glucosidase enzymatic activities. Our survey led to the identification of promising molecular scaffolds such as compounds **A** and **B**, which contain key pharmacophores including acetamide, indole, benzo[*d*]imidazole, or carboxylic acid moieties within their structures (Fig. 1).[11,12] Notably, with the exception of the carboxylic acid group, other latter pharmacophores are also consistently present in potent α-glucosidase inhibitors such as compounds **C** and **D** (Fig. 1).[13,14] It should also be noted that each of these representative compounds (**A–D**) was reported as the most potent inhibitor within its respective structural classes. Guided by these observations, we

[a]*Center for Research of Endemic Parasites of Iran, Tehran University of Medical Sciences, Tehran, Iran*
[b]*School of Chemistry, College of Science, University of Tehran, Tehran, Iran*
[c]*Endocrinology and Metabolism Research Center, Endocrinology and Metabolism Clinical Sciences Institute, Tehran University of Medical Sciences, Tehran, Iran. E-mail: momahdavi@tums.ac.ir*
[d]*Department of Biology, Babol Branch, Islamic Azad University, Babol, Iran*
[e]*Department of Pharmaceutical Chemistry, School of Pharmacy, Shahid Beheshti University of Medical Sciences, Tehran, Iran*
[f]*Department of Pharmaceutical Biotechnology, Faculty of Pharmacy and Biotechnology Research Center, Tehran University of Medical Sciences, Tehran, Iran*
[g]*Department of Medicinal Chemistry, Faculty of Pharmacy, Tehran University of Medical Sciences, Tehran, Iran*
[h]*Cellular and Molecular Biology Research Center, Health Research Institute, Babol University of Medical Sciences, Babol, Iran. E-mail: maryammoha@gmail.com*

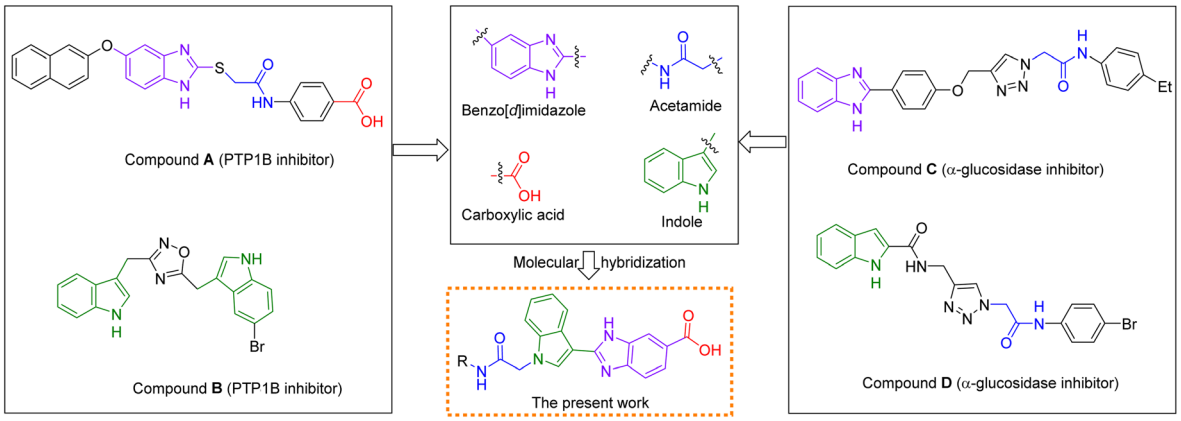

Fig. 1 Design strategy for new acetamide–indole–benzo[*d*]imidazole–carboxylic acid hybrids as new dual PTP1B/α-glucosidase inhibitors.

rationally designed a new series of acetamide–indole–benzo[*d*]imidazole–carboxylic acid hybrids and synthesized fourteen derivatives **8a–n** through conventional organic synthesis methodologies. Notably, our integrated acetamide–indole–benzo[*d*]imidazole–carboxylic acid hybrid represents a previously unreported scaffold in dual PTP1B/α-glucosidase inhibition, thereby exploring novel chemical space for multi-target anti-diabetic drug discovery. These synthesized compounds were evaluated for their inhibitory activity against both PTP1B and α-glucosidase.

Materials and methods

Synthesis of indole-3-carboxaldehyde (2)

Phosphorus oxychloride (340 mmol) was added dropwise to DMF (50 mL), while cooled at 0–5 °C, and stirred in an ice bath for 1 h. Then, indole (**1**, 170 mmol dissolved in 15 mL of DMF) was added to the ice-cold mixture and the reaction was continued at 25 °C for 2 h. After that, the mixture was poured into ice water (600 mL) and NaOH was added to adjust the pH to 8.0 was added to mixture. The crude product was filtered off and washed with water to obtain indole-3-carboxaldehyde (**2**).[15]

General synthesis for 2-chloroacetamide derivatives 5a–n

A mixture of aniline derivatives **3a–n** (2 mmol) and chloroacetyl chloride (**4**) (2 mmol) in DMF (10 mL) was stirred at room temperature for 24 h. The reaction mixture was then diluted with cold water and poured onto ice. The resulting precipitate was filtered, washed with cold water, and dried to afford pure 2-chloroacetamide derivatives **5a–n**.[16]

General synthesis for acetamide–indole–carboxylic acid derivatives 6a–n

A mixture of indole-3-carboxaldehyde (**2**) (1 mmol), 2-chloroacetamide derivatives **5a–n** (1.2 mmol) in dry acetone (10 mL) and anhydrous K_2CO_3 (1 mmol) was stirred at room temperature for 4 h, filtered, and the resulting solid was recrystallized from ethanol to give the final products **6a–n**.[17]

General synthesis for acetamide–indole–benzo[*d*]imidazole–carboxylic acid derivatives 8a–n

Compounds **6a–n** (1 mmol) and 3,4-diaminobenzoic acid (**7**, 1.2 mmol) along with a catalytic amount of $Na_2S_2O_5$ were dissolved in DMF (10 mL) and the mixture was stirred at 150 °C for 24 h. Upon completion of the reaction (as monitored by TLC), H_2O (20 mL) was added to the reaction mixture, it was filtered, and recrystallized to give the target compounds **8a–n**.[18]

2-(1-(2-Oxo-2-(phenylamino)ethyl)-1*H*-indol-3-yl)-1*H*-benzo[*d*]imidazole-6-carboxylic acid (8a). Cream solid; yield: 78%; MP = 151–153 °C; ^{1}H NMR (400 MHz, DMSO-d_6) δ 10.58 (s, 1H), 8.44 (d, J = 9.3 Hz, 1H), 8.39 (s, 1H), 8.20 (s, 1H), 7.94 (d, J = 8.5 Hz, 1H), 7.73 (d, J = 8.4 Hz, 1H), 7.63 (d, J = 7.1 Hz, 2H), 7.37 (t, J = 5.1 Hz, 3H), 7.33 (d, J = 7.3 Hz, 2H), 7.09 (t, J = 7.3 Hz, 1H), 5.31 (s, 2H); ^{13}C NMR (101 MHz, DMSO-d_6) δ 167.95, 166.03, 162.79, 139.06, 137.71, 133.73, 129.40, 125.80, 125.17, 124.88, 124.19, 123.72, 122.09, 121.29, 119.64, 116.58, 115.70, 115.55, 111.42, 50.04; anal. calcd: $C_{24}H_{18}N_4O_3$; C, 70.23; H, 4.42; N, 13.65; found; C, 70.32; H, 4.51; N, 13.79.

2-(1-(2-Oxo-2-(*o*-tolylamino)ethyl)-1*H*-indol-3-yl)-1*H*-benzo[*d*]imidazole-6-carboxylic acid (8b). Cream solid; yield: 81%; MP = 163–165 °C; ^{1}H NMR (400 MHz, DMSO-d_6) δ 9.90 (s, 1H), 8.46 (d, J = 8.8 Hz, 1H), 8.41 (s, 1H), 8.20 (s, 1H), 7.93 (d, J = 6.9 Hz, 1H), 7.72 (d, J = 8.4 Hz, 1H), 7.67 (d, J = 8.9 Hz, 1H), 7.45 (d, J = 7.8 Hz, 1H), 7.41–7.34 (m, 2H), 7.24 (d, J = 7.4 Hz, 1H), 7.18 (t, J = 7.5 Hz, 1H), 7.11 (t, J = 7.3 Hz, 1H), 5.35 (s, 2H), 2.27 (s, 3H); ^{13}C NMR (101 MHz, DMSO-d_6) δ 168.00, 166.18, 162.79, 150.36, 137.64, 136.15, 133.67, 132.16, 130.93, 126.54, 126.03, 125.68, 125.27, 124.77, 123.65, 122.06, 121.39, 116.76–114.95 (m), 114.07, 111.33, 103.41, 49.81, 18.38; anal. calcd: $C_{25}H_{20}FN_4O_3$; C, 70.74; H, 4.75; N, 13.20; found; C, 70.92; H, 4.71; N, 13.29.

2-(1-(2-Oxo-2-(*m*-tolylamino)ethyl)-1*H*-indol-3-yl)-1*H*-benzo[*d*]imidazole-6-carboxylic acid (8c). Cream solid; yield: 66%; MP = 146–148 °C; ^{1}H NMR (400 MHz, DMSO-d_6) δ 10.52 (s, 1H), 8.45 (d, J = 9.2 Hz, 1H), 8.40 (s, 1H), 8.21 (s, 1H), 7.94 (d, J = 6.9 Hz, 1H), 7.73 (d, J = 8.4 Hz, 1H), 7.66–7.61 (m, 1H), 7.47 (s, 1H), 7.42 (d, J = 8.3 Hz, 1H), 7.37–7.35 (m, 2H), 7.22 (t, J = 7.8 Hz, 1H), 6.91 (d, J = 7.5 Hz, 1H), 5.30 (s, 2H), 2.28 (s, 3H); ^{13}C NMR (101 MHz, DMSO-d_6) δ 167.96, 165.95, 150.26, 138.99, 138.58, 137.70,

133.77, 129.22, 125.80, 125.18, 124.88, 123.70, 122.08, 121.29, 120.21, 116.86, 115.70, 114.11, 111.41, 103.22, 50.08, 21.65; anal. calcd: $C_{25}H_{20}N_4O_3$; C, 70.74; H, 4.75; N, 13.20; found; C, 70.92; H, 4.81; N, 13.25.

2-(1-(2-Oxo-2-(*p*-tolylamino)ethyl)-1*H*-indol-3-yl)-1*H*-benzo[*d*]imidazole-6-carboxylic acid (8d). Cream solid; yield: 71%; MP = 157–159 °C; ^{1}H NMR (400 MHz, DMSO-d_6) δ 10.48 (s, 1H), 8.49 (d, J = 9.2 Hz, 1H), 8.32 (s, 1H), 8.17 (s, 1H), 7.88 (d, J = 6.8 Hz, 1H), 7.68 (d, J = 8.4 Hz, 1H), 7.64–7.58 (m, 1H), 7.52 (d, J = 8.5 Hz, 2H), 7.36–7.30 (m, 2H), 7.14 (d, J = 8.2 Hz, 2H), 5.26 (s, 2H), 2.26 (s, 3H); ^{13}C NMR (101 MHz, DMSO-d_6) δ 168.22, 165.91, 162.79, 151.01, 137.66, 136.57, 133.12, 132.75, 129.75, 125.54, 125.00, 124.20, 123.43, 121.76, 121.65, 119.67, 111.15, 104.66, 49.96, 20.93; anal. calcd: $C_{25}H_{20}N_4O_3$; C, 70.74; H, 4.75; N, 13.20; found; C, 70.87; H, 4.93; N, 13.39.

2-(1-(2-((2,3-Dimethylphenyl)amino)-2-oxoethyl)-1*H*-indol-3-yl)-1*H*-benzo[*d*]imidazole-6-carboxylic acid (8e). Cream solid; yield: 67%; MP = 159–161 °C; ^{1}H NMR (400 MHz, DMSO-d_6) δ 9.94 (s, 1H), 8.50 (d, J = 8.9 Hz, 1H), 8.33 (s, 1H), 8.16 (s, 1H), 7.88 (d, J = 6.9 Hz, 1H), 7.68–7.64 (m, 2H), 7.38–7.31 (m, 2H), 7.19 (d, J = 6.8 Hz, 1H), 7.09–7.02 (m, 2H), 5.31 (s, 2H), 2.26 (s, 3H), 2.13 (s, 3H); ^{13}C NMR (101 MHz, DMSO-d_6) δ 168.22, 166.35, 162.79, 151.03, 137.62, 137.59, 135.91, 132.76, 132.74, 131.56, 127.73, 125.77, 125.61, 124.98, 124.19, 123.79, 123.41, 121.77, 114.38, 114.18, 111.09, 106.13, 49.72, 20.63, 14.56; anal. calcd: $C_{26}H_{22}N_4O_3$; C, 71.22; H, 5.06; N, 12.78; found; C, 71.32; H, 5.19; N, 12.84.

2-(1-(2-((2,4-Dimethoxyphenyl)amino)-2-oxoethyl)-1*H*-indol-3-yl)-1*H*-benzo[*d*]imidazole-6-carboxylic acid (8f). Cream solid; yield: 70%; MP = 165–167 °C; ^{1}H NMR (400 MHz, DMSO-d_6) δ 12.74–12.37 (m, 2H), 9.62 (s, 1H), 8.54 (d, J = 8.8 Hz, 1H), 8.25 (s, 1H), 8.14 (s, 1H), 7.83 (d, J = 8.1 Hz, 1H), 7.74 (d, J = 8.8 Hz, 1H), 7.63 (t, J = 8.5 Hz, 2H), 7.34–7.27 (m, 2H), 6.66 (d, J = 2.6 Hz, 1H), 6.48 (dd, J = 8.9, 2.7 Hz, 1H), 5.30 (s, 2H), 3.86 (s, 3H), 3.74 (s, 3H); ^{13}C NMR (101 MHz, DMSO-d_6) δ 168.44, 166.19, 162.79, 157.43, 151.73, 137.55, 131.84, 125.88, 124.31, 123.68, 123.18, 121.96, 121.49, 120.26, 110.98, 105.88, 104.51, 99.34, 56.27, 55.76, 49.80; anal. calcd: $C_{26}H_{22}N_4O_5$; C, 66.38; H, 4.71; N, 11.91; found; C, 66.42; H, 4.84; N, 12.08.

2-(1-(2-((4-Ethylphenyl)amino)-2-oxoethyl)-1*H*-indol-3-yl)-1*H*-benzo[*d*]imidazole-6-carboxylic acid (8g). Cream solid; yield: 84%; MP = 158–160 °C; ^{1}H NMR (400 MHz, DMSO-d_6) δ 10.48 (s, 1H), 8.55 (d, J = 8.9 Hz, 1H), 8.24 (s, 1H), 8.14 (s, 1H), 7.82 (d, J = 6.8 Hz, 1H), 7.62 (d, J = 8.3 Hz, 1H), 7.58–7.55 (m, 1H), 7.54 (d, J = 8.4 Hz, 2H), 7.32–7.27 (m, 2H), 7.17 (d, J = 8.4 Hz, 2H), 5.23 (s, 2H), 2.56 (q, J = 7.6 Hz, 2H), 1.15 (t, J = 7.6 Hz, 3H); ^{13}C NMR (101 MHz, DMSO-d_6) δ 168.50, 166.06, 139.57, 137.60, 136.78, 131.67, 128.56, 125.95, 124.17, 123.50, 123.15, 122.04, 121.43, 119.76, 110.85, 106.19, 49.92, 28.07, 16.16; anal. calcd: $C_{26}H_{22}N_4O_3$; C, 71.22; H, 5.06; N, 12.78; found; C, 71.32; H, 5.23; N, 12.96.

2-(1-(2-((2-Fluorophenyl)amino)-2-oxoethyl)-1*H*-indol-3-yl)-1*H*-benzo[*d*]imidazole-6-carboxylic acid (8h). Cream solid; yield: 68%; MP = 172–174 °C; ^{1}H NMR (400 MHz, DMSO-d_6) δ 12.99–12.73 (m, 1H), 12.64 (s, 1H), 10.36 (s, 1H), 8.56 (d, J = 8.9 Hz, 1H), 8.28–8.20 (m, 1H), 7.97–7.91 (m, 1H), 7.82 (t, J = 8.7 Hz, 1H), 7.73–7.51 (m, 2H), 7.36–7.30 (m, 2H), 7.29–7.26 (m, 1H), 7.20–7.15 (m, 2H), 5.35 (s, 2H); ^{13}C NMR (101 MHz, DMSO-d_6) δ 168.58, 168.45, 166.96, 155.16, 152.72, 152.29, 151.52–150.88 (m), 148.25, 144.39, 138.19, 137.59, 134.41, 131.71, 131.44, 126.22, 126.10, 125.98, 125.00, 124.97, 124.20, 124.13, 123.18, 122.09, 121.45, 120.03, 117.88, 116.18, 115.99, 112.49, 110.81, 110.59, 106.38, 49.66; anal. calcd: $C_{24}H_{17}FN_4O_3$; C, 67.28; H, 4.00; N, 13.08; found; C, 67.39; H, 4.16; N, 13.21.

2-(1-(2-((3-Chlorophenyl)amino)-2-oxoethyl)-1*H*-indol-3-yl)-1*H*-benzo[*d*]imidazole-6-carboxylic acid (8i). Brown solid; yield: 79%; MP = 174–176 °C; ^{1}H NMR (400 MHz, DMSO-d_6) δ 10.15 (s, 1H), 8.45 (d, J = 8.9 Hz, 1H), 8.40 (s, 1H), 8.20 (s, 1H), 7.93 (d, J = 8.5 Hz, 1H), 7.76 (d, J = 8.1 Hz, 1H), 7.73 (d, J = 8.5 Hz, 1H), 7.66 (d, J = 7.9 Hz, 1H), 7.54 (d, J = 8.0 Hz, 1H), 7.40–7.37 (m, 1H), 7.36–7.32 (m, 2H), 7.23 (t, J = 8.5 Hz, 1H), 5.42 (s, 2H); ^{13}C NMR (101 MHz, DMSO-d_6) δ 167.99, 166.73, 150.31, 137.63, 134.78, 133.62, 130.12, 128.06, 127.22, 126.89, 126.40, 125.70, 125.26, 124.79, 123.71, 122.10, 121.38, 115.78, 114.13, 111.36, 103.55, 49.79; anal. calcd: $C_{24}H_{17}ClN_4O_3$; C, 64.80; H, 3.85; N, 12.59; found; C, 64.97; H, 3.91; N, 12.71.

2-(1-(2-((4-Chlorophenyl)amino)-2-oxoethyl)-1*H*-indol-3-yl)-1*H*-benzo[*d*]imidazole-6-carboxylic acid (8j). Brown solid; yield: 63%; MP = 177–179 °C; ^{1}H NMR (400 MHz, DMSO-d_6) δ 10.74 (s, 1H), 8.46 (d, J = 9.1 Hz, 1H), 8.36 (s, 1H), 8.19 (s, 1H), 7.92 (d, J = 6.9 Hz, 1H), 7.71 (d, J = 8.4 Hz, 1H), 7.67 (d, J = 8.9 Hz, 2H), 7.67–7.60 (m, 1H), 7.40 (d, J = 8.8 Hz, 2H), 7.36–7.34 (m, 2H), 5.31 (s, 2H); ^{13}C NMR (101 MHz, DMSO-d_6) δ 168.05, 166.31, 150.49, 138.03, 137.71, 133.39, 129.31, 127.72, 125.53, 125.29, 124.65, 123.63, 121.99, 121.41, 121.23, 115.77, 114.19, 114.00, 111.34, 103.80, 49.99; anal. calcd: $C_{24}H_{17}ClN_4O_3$; C, 64.80; H, 3.85; N, 12.59; found; C, 64.87; H, 3.92; N, 12.61.

2-(1-(2-((4-Bromophenyl)amino)-2-oxoethyl)-1*H*-indol-3-yl)-1*H*-benzo[*d*]imidazole-6-carboxylic acid (8k). Cream solid; yield: 72%; MP = 178–180 °C; ^{1}H NMR (400 MHz, DMSO-d_6) δ 10.72 (s, 1H), 8.52 (d, J = 9.3 Hz, 1H), 8.29 (s, 1H), 8.17 (s, 1H), 7.86 (d, J = 8.4 Hz, 1H), 7.66 (d, J = 8.3 Hz, 1H), 7.65–7.57 (m, 3H), 7.53 (d, J = 8.9 Hz, 2H), 7.31 (t, J = 5.4 Hz, 2H), 5.28 (s, 2H); ^{13}C NMR (101 MHz, DMSO-d_6) δ 168.33, 166.49, 162.80, 151.27, 138.46, 137.66, 132.34, 132.21, 125.68, 124.71, 123.96, 123.36, 121.80, 121.66, 121.61, 115.76, 114.18, 111.06, 49.94; anal. calcd: $C_{24}H_{17}N_4O_3$; C, 58.91; H, 3.50; N, 11.45; found; C, 59.07; H, 3.63; N, 11.57.

2-(1-(2-((4-Nitrophenyl)amino)-2-oxoethyl)-1*H*-indol-3-yl)-1*H*-benzo[*d*]imidazole-6-carboxylic acid (8l). Cream solid; yield: 72%; MP = 187–189 °C; ^{1}H NMR (400 MHz, DMSO-d_6) δ 11.19 (s, 1H), 8.55 (d, J = 9.0 Hz, 1H), 8.30–8.23 (m, 3H), 8.17 (s, 1H), 7.89 (d, J = 9.2 Hz, 2H), 7.85 (d, J = 8.3 Hz, 1H), 7.65 (d, J = 8.4 Hz, 1H), 7.62–7.59 (m, 1H), 7.32–7.30 (m, 2H), 5.36 (s, 2H); ^{13}C NMR (101 MHz, DMSO-d_6) δ 168.43, 167.49, 151.51, 145.23, 142.95, 137.69, 131.94, 125.81, 125.62, 124.45, 123.73, 123.30, 121.93, 121.58, 119.46, 119.33, 116.17, 114.33, 111.01, 105.96, 49.99; anal. calcd: $C_{24}H_{17}N_5O_5$; C, 63.29; H, 3.76; N, 15.38; found; C, 63.47; H, 3.94; N, 15.56.

2-(1-(2-(Benzylamino)-2-oxoethyl)-1*H*-indol-3-yl)-1*H*-benzo[*d*]imidazole-6-carboxylic acid (8m). Cream solid; yield: 87%; MP = 144–146 °C; ^{1}H NMR (400 MHz, DMSO-d_6) δ 8.95 (t, J = 5.9 Hz, 1H), 8.43 (d, J = 6.0 Hz, 1H), 8.38 (s, 1H), 8.20 (s, 1H), 7.95 (d, J = 6.9 Hz, 1H), 7.74 (d, J = 8.4 Hz, 1H), 7.63–7.55 (m, 1H), 7.38–7.36 (m, 1H), 7.36–7.34 (m, 2H), 7.34–7.31 (m, 3H), 7.30–7.27 (m,

1H), 5.16 (s, 2H), 4.36 (d, J = 5.8 Hz, 2H); ^{13}C NMR (101 MHz, DMSO-d_6) δ 167.91, 167.20, 150.12, 139.34, 137.57, 133.92, 128.84, 127.84, 127.47, 125.94, 125.14, 124.99, 123.65, 122.14, 121.24, 115.65, 114.07, 111.42, 102.87, 49.55, 42.88; anal. calcd: $C_{25}H_{20}N_4O_3$; C, 70.74; H, 4.75; N, 13.20; found; C, 70.89; H, 4.79; N, 13.37.

2-(1-(2-Oxo-2-(phenethylamino)ethyl)-1*H*-indol-3-yl)-1*H*-benzo[*d*]imidazole-6-carboxylic acid (8n). Cream solid; yield: 63%; MP = 160–162 °C; ^{1}H NMR (400 MHz, DMSO-d_6) δ 12.88 (s, 1H), 12.64 (s, 1H), 8.56–8.53 (m, 1H), 8.45 (t, J = 5.7 Hz, 1H), 8.18 (s, 1H), 8.14 (s, 1H), 7.82 (d, J = 6.8 Hz, 1H), 7.62 (d, J = 8.2 Hz, 1H), 7.47–7.38 (m, 1H), 7.32–7.29 (m, 2H), 7.29–7.25 (m, 2H), 7.25–7.21 (m, 2H), 7.21–7.20 (m, 1H), 4.97 (s, 2H), 3.40–3.32 (m, 2H), 2.76 (t, J = 7.2 Hz, 2H); ^{13}C NMR (101 MHz, DMSO-d_6) δ 168.51, 167.33, 139.71, 137.39, 131.57, 129.17, 128.83, 126.64, 125.99, 124.12, 123.46, 123.04, 122.04, 121.38, 110.82, 106.13, 49.46, 40.86, 35.45; anal. calcd: $C_{26}H_{22}N_4O_3$; C, 71.22; H, 5.06; N, 12.78; found; C, 71.40; H, 5.23; N, 12.91.

PTP1B inhibition assay

The inhibitory activity of the newly synthesized compounds **8a–n** against human recombinant PTP1B was assessed using a spectrophotometric assay in a microplate format. Each test compound was dissolved in PTP1B assay buffer, which consisted of 100 mM HEPES (pH 7.2), 2 mM EDTA, 2 mM DTT, and 0.1% nonylphenyl polyethylene glycol, with a final volume of 45 μL per well. Following a 10-minute pre-incubation at 30 °C, the enzymatic reaction was initiated by adding 5 μL of enzyme (final concentration: 3.5 ng mL^{-1}) and 50 μL of the phosphopeptide substrate IR5 (0.75 μM). After 25 minutes of incubation at 30 °C, the reaction was terminated by the addition of 10 μL of a red reagent. The released orthophosphate, resulting from the dephosphorylation of IR5 by PTP1B, was quantified by measuring the absorbance at 620 nm after a 20-minute incubation. The known PTP1B inhibitor suramin was used as a positive control. For the IC_{50} determinations, all experiments were performed in triplicate (n = 3). The IC_{50} values were calculated by nonlinear regression using logarithmic dose–response curve fitting.

α-Glucosidase inhibition assay

The inhibitory activity of the synthesized acetamide–indole–benzimidazole–carboxylic acid derivatives (**8a–n**) was evaluated against *Saccharomyces cerevisiae* α-glucosidase (EC 3.2.1.20). The enzyme was prepared in potassium phosphate buffer (PPB, 50 mM, pH 6.8), while the test compounds were dissolved in DMSO, achieving a final concentration of 10% in the assay mixture. The reaction was conducted in a 96-well plate, where a mixture of 135 μL of PPB, 20 μL of the enzyme solution, and 20 μL of a test compound at varying concentrations was pre-incubated for 10 minutes at 37 °C. The enzymatic reaction was then initiated by adding 25 μL of the substrate, *p*-nitrophenyl glucopyranoside (4 mM). After an additional 25 minutes of incubation at 37 °C, the absorbance was measured at 405 nm using a BioTek Gen5 PowerWave XS2 microplate reader. The release of *p*-nitrophenol was quantified to determine the inhibitory potential of the compounds. All experiments were performed in triplicate (n = 3) for the determination of IC_{50} values. These values were calculated by nonlinear regression using logarithmic dose–response curve fitting.

Kinetic study against PTP1B

The inhibition type of the most active PTP1B inhibitor was investigated at different substrate concentrations (IR5, 0.075–0.750 μM) in the absence and presence of the inhibitor at various concentrations (0.6, 1.1, and 2.2 μM). Lineweaver–Burk plots were generated to determine the inhibition type, and the Michaelis–Menten constant (K_m) was determined from the relationship between the reciprocal of substrate concentration (1/[S]) and the reciprocal of the enzyme reaction rate (1/V) across different inhibitor concentrations.

Docking study in the active site of PTP1B

Docking studies against PTP1B (pdb code: 2QBS) were performed by Autodock Tools 1.5.6.[19] The 3D structures of the selected compounds (the standard inhibitor, the co-crystallized ligand, and the most potent compounds) were constructed by MarvinSketch 5.10.4, and then the pdbqt format of these ligands were prepare by Autodock Tools 1.5.6. The enzyme structure was also prepared in pdbqt format using the same software. The docking grid box was set to 60 × 60 × 60 Å, centered at X = 49.28, Y = 12.106, Z = 4.338. Each docked system was carried out by 20 runs of the Autodock search (by the Lamarckian genetic algorithm). Finally, according to obtain BE values, the best-docked pose of each inhibitor was selected and analyzed by Discovery Studio 2019 Client (Accelrys, Inc., San Diego, CA).

Molecular dynamics on PTP1B–ligand complexes

The molecular dynamics (MD) simulations of PTP1B–ligand complexes were performed using GROMACS 5.1.2 on Ubuntu 18.04.5 LTS.[20] Topology and force field parameters for the ligands were generated using the SwissParam server, which provides parameter files compatible with the CHARMM all-atom force field for small organic molecules.[21] The protein topology was generated using the pdb2gmx command in GROMACS with the CHARMM27 all-atom force field (CHARMM22 plus CMAP for proteins). The ligand topology files (.itp) generated by SwissParam were incorporated into the protein topology (.top) file, and the corresponding GROMACS-formatted (.gro) files of the protein and ligands were merged using Notepad++.

The protein–ligand complex was centered within a cubic simulation box, ensuring a 1.0 nm clearance from the box edges. Solvation was carried out using the SPC216 water model, and 5 water molecules were replaced by Na^+ ions to neutralize the net negative charge of the system. Energy minimization was conducted using the steepest descent algorithm for up to 50 000 steps, reducing the maximum force to below 10.0 kJ mol^{-1}. The system underwent equilibration in two stages. *NVT* equilibration was performed at 300 K for 500 ps using the V-rescale thermostat with a coupling constant of 0.1 ps. This was followed by *NPT* equilibration for 1000 ps using the Berendsen pressure coupling algorithm with a coupling constant of 5.0 ps.

Long-range electrostatic interactions were treated using the Particle-Mesh Ewald (PME) method with a cutoff of 1.0 nm for electrostatics. van der Waals interactions were calculated using a 1.2 nm cutoff. After these preparatory steps, a 20 ns MD simulation was performed to investigate the stability and dynamic behavior of the protein–ligand complex.

In silico ADMET, drug-likeness, and bioavailability studies

The ADMET properties of the selected compounds were predicted *in silico* using the pkCSM online server.[22] Furthermore, drug-likeness and oral bioavailability of these compounds were assessed with the admetSAR and SwissADME web tools, respectively.[23,24]

Result and discussion

Chemistry

The synthetic pathway employed to access the new acetamide–indole–benzo[*d*]imidazole–carboxylic acid derivatives **8a–n** is outlined in Scheme 1.[15–18] The synthesis started with the Vilsmeier formylation of indole (**1**), providing indole-3-carboxaldehyde (**2**). Concurrently, a series of 2-chloroacetamide derivatives **5a–n** were prepared by reacting various aniline derivatives **3a–n** with chloroacetyl chloride (**4**). The subsequent step involved the reaction of indole-3-carboxaldehyde (**2**) with compounds **5a–n** to give the acetamide–indole–carboxylic acid derivatives **6a–n**. The final target compounds **8a–n** were efficiently constructed *via* a reaction between compounds **6a–n** and 3,4-diaminobenzoic acid (**7**).

Anti-PTP1B assay of new compounds 8a–n

The inhibitory activities of the acetamide–indole–benzo[*d*]imidazole–carboxylic acid derivatives **8a–n** against human recombinant PTP1B were evaluated, and the corresponding IC_{50} values are summarized in Table 1. The results indicate a significant range of potency, with IC_{50} values varying from the micromolar to the inactive range ($IC_{50} > 10$ μM). Notably, compound **8l** emerged as the most potent PTP1B inhibitor in this series ($IC_{50} = 2.2$ μM), displaying an approximately 4.5-fold increase in potency compared to the standard inhibitor, suramin ($IC_{50} = 10.0$ μM).

As can be seen in Scheme 1 and Table 1, most of the newly synthesized compounds feature an acetamide moiety substituted with various R groups. These R groups are phenyl derivatives in compounds **8a–l**, a benzyl derivative in compound **8m**, and a phenethyl derivative in compound **8n**. As expected, the structure–activity relationship (SAR) analysis reveals that the nature of this R group is a critical determinant for the observed PTP1B inhibitory activity. SAR analysis of compounds **8a–n** is schematically depicted in Fig. 2.

SAR analysis of compounds **8a–n** showed that all active PTP1B inhibitors belong to the *N*-phenylacetamide series. The most potent compound was the 4-nitro derivative **8l** ($IC_{50} = 2.2$ μM). As shown in Fig. 2, inhibitory potency for 4-substituted derivatives followed the order: NO_2 > Et (**8g**, $IC_{50} = 5.9$ μM) > Cl (**8j**, $IC_{50} = 6.7$ μM) > Me (**8d**, $IC_{50} = 8.1$ μM) > Br (**8k**, inactive). All these substituted compounds, with the exception of 4-bromo derivative, were more active than the un-substituted analogue **8a** ($IC_{50} = 10.0$ μM), underscoring the importance of the 4-position. This trend is further reinforced by the activity of the 2,4-dimethyl derivative **8f** ($IC_{50} = 3.8$ μM), the third most potent compound. Here, the favorable 4-methyl group appears to offset the steric hindrance from the 2-methyl, while the mono-2-methyl analogue was inactive (**8b**). On the other hand, the inactivity of the 4-bromo analogue (**8k**) suggests that its larger atomic radius and potential steric crowding may impair optimal binding within the enzyme's active site. The second potent compound was 2-fluoro derivative **8h** while other 2-substituted analogs like compound **8b** and compound **8e** (2,3-diMe) were inactive ($IC_{50} > 10$ μM), underscoring that the steric tolerance is highly specific to the very small fluorine atom. Both 3-substituted compounds, 3-methyl derivative **8b** and 3-chloro derivative **8i** were also inactive against PTP1B. In summary, the observed SAR in *N*-phenylacetamide for the synthesized derivatives demonstrates that, in addition to whether the substituents are electron-donating or electron-withdrawing, their precise positions on the phenyl ring critically govern the inhibitory potency.

Table 1 and Fig. 2 also demonstrate that replacing the rigid phenyl ring of compound **8a** with flexible alkyl chains bearing a terminal phenyl group, as in the cases of compounds **8m** (–CH_2-Ph) and **8n** (–CH_2–CH_2-Ph), completely abolishes activity.

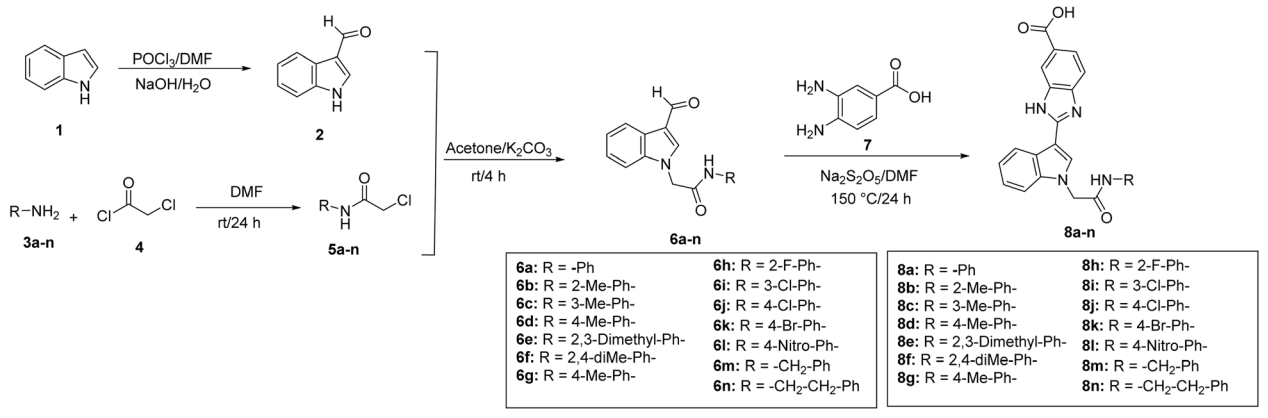

Scheme 1 Synthetic procedure for acetamide–indole–benzo[*d*]imidazole–carboxylic acid derivatives **8a–n**.

Table 1 Anti-PTP1B inhibitory activity of the target compounds **8a–n**

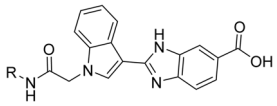

Compound	R	IC_{50} (μM)	Compound	R	IC_{50} (μM)
8a	-Ph	10.0 ± 0.2	**8h**	2-F-Ph-	3.1 ± 0.1
8b	2-Me-Ph-	>10	**8i**	3-Cl-Ph-	>10
8c	3-Me-Ph-	>10	**8j**	4-Cl-Ph-	6.7 ± 0.3
8d	4-Me-Ph-	8.1 ± 0.2	**8k**	4-Br-Ph-	>10
8e	2,3-diMe-Ph-	>10	**8l**	4-NO_2-Ph-	2.2 ± 0
8f	2,4-diMe-Ph-	3.8 ± 0.1	**8m**	–CH_2-Ph	>10
8g	4-Et-Ph-	5.9 ± 0.1	**8n**	–CH_2–CH_2-Ph	>10
Suramin	—	10.0 ± 0.2	Suramin	—	10.0 ± 0.2

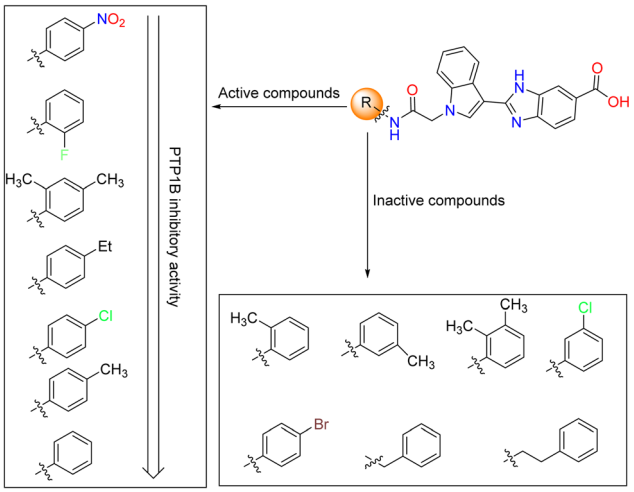

Fig. 2 SAR analysis of compounds **8a–n** against PTP1B.

Anti-α-glucosidase assay of new compounds 8a–n

Given the presence of known pharmacophores effective against α-glucosidase and the enzyme's key role in diabetes treatment, the newly synthesized compounds (**8a–n**) were evaluated for this activity. The obtained inhibition percentages are listed in Table 2. The data reveal that all new compounds were less potent than acarbose, except for the 4-bromo (compound **8k**, 60% inhibition) and 4-chloro (compound **8j**, 54% inhibition) derivatives.

Analysis of the structure–activity relationship (SAR) for compounds **8a–l** (R = phenyl derivatives) indicates significant steric hindrance at the 2-position of the phenyl ring. Any substitution at this position, as in compounds **8b** (2-Me), **8e** (2,3-diMe), **8f** (2,4-diMe), and **8h** (2-F), leads to inactivity or a significant loss of potency. In contrast, 4-substituted derivatives consistently exhibited moderate to good activity, with the 4-Br (compound **8k**, 60% inhibition, IC_{50} = 551.43 μM), 4-Cl (compound **8j**, 54% inhibition, IC_{50} = 659.98 μM), and 4-NO_2 (compound **8l**, 40% inhibition) groups being particularly favorable.

The data further demonstrate that both the *N*-phenylacetamide (compound **8a**) and *N*-benzylacetamide (compound **8m**) derivatives were inactive against α-glucosidase. Conversely, the *N*-phenethylacetamide derivative (compound **8n**, 40% inhibition) exhibited moderate activity against this enzyme.

Comparison of SAR between anti-PTP1B and anti-α-glucosidase assays

As shown in Table 1, the most potent compound against PTP1B is the 4-nitro derivative **8l**. Interestingly, this same compound is also the third most potent against α-glucosidase. The top two inhibitors of α-glucosidase are the 4-bromo and 4-chloro derivatives, **8k** and **8j**, respectively. Notably, while the 4-chloro derivative (**8j**) exhibits clear activity against PTP1B, its bromo analogue (**8k**) shows no significant inhibition of this enzyme. Overall, this comparative analysis suggests that electron-withdrawing groups enhance inhibitory activity against both enzymes, although with distinct selectivity profiles influenced by the specific halogen substituent.

Kinetic study against PTP1B

The kinetic analysis of compound **8l** against PTP1B was performed and its inhibition mechanism was determined by the characteristic Lineweaver–Burk plot pattern (Fig. 3a). This plot pattern indicates that **8l** binds directly to the enzyme's active site and competes with the substrate. The inhibition constant (K_i) was determined to be 2.2 μM (Fig. 3b). The competitive nature of compound **8l**, along with its high inhibitory potency, suggests that it effectively inhibits PTP1B catalytic activity by blocking substrate access to the active site.

Docking study in the active site of PTP1B

Molecular docking was performed to explore the binding modes of the newly synthesized potent compounds within the active site of PTP1B. The crystal structure of PTP1B (PDB ID: 2QBS) was obtained from the Protein Data Bank (PDB) for this purpose. The co-crystallized ligand in this PTP1B structure is 4-bromo-3-(carboxymethoxy)-5-[3-(cyclohexylamino)phenyl] thiophene-2-carboxylic acid (listed as compound **024** in the PDB). For docking validation, this native ligand was re-docked.

Table 2 α-Glucosidase inhibitory activities of the target compounds **8a–n**

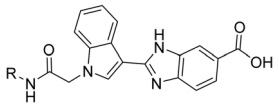

Compound	R	% inhibition	IC_{50} (μM)	Compound	R	% inhibition	IC_{50} (μM)
8a	-Ph	1 ± 0.84	>750	**8h**	2-F-Ph-	0	>750
8b	2-Me-Ph-	5 ± 0.63	>750	**8i**	3-Cl-Ph-	3 ± 0.27	>750
8c	3-Me-Ph-	19 ± 0.44	>750	**8j**	4-Cl-Ph-	54 ± 0.19	659.98 ± 1.26
8d	4-Me-Ph-	34 ± 0.57	>750	**8k**	4-Br-Ph-	60 ± 0.32	551.43 ± 0.95
8e	2,3-diMe-Ph-	0	>750	**8l**	4-NO_2-Ph-	40 ± 0.21	>750
8f	2,4-diMe-Ph-	6 ± 0.58	>750	**8m**	–CH_2-Ph	0	>750
8g	4-Et-Ph-	28 ± 0.42	>750	**8n**	–CH_2–CH_2-Ph	40 ± 0.73	>750
Acarbose	—	50 ± 0.12	750.3 ± 0.67	Acarbose	—	50 ± 0.12	750.3 ± 0.67

Subsequently, our novel compounds and the standard inhibitor, suramin, were docked into the active site.

Fig. 4a illustrates the superimposed conformer of the native co-crystallized ligand (compound **024**), the standard inhibitor suramin, and the most potent synthesized compound (**8l**). Interaction modes of these compounds are shown in Fig. 4b and c.

As can be seen in Fig. 4b, compound **024** established six hydrogen bonds with residues Ser215, Cys214, Arg220, Phe181, Gln265, and Gln261. This ligand formed an unfavorable interaction with Arg220. Compound **024** also established a π–sigma interaction with Ala216 and several hydrophobic interactions with Val48, Ilu218, Ala216, and Met257. The binding energy (BE) value of compound **024** in the active site of PTP1B was −10.89 kcal mol^{-1}.

Suramin established five classical hydrogen bonds with residues Ser27, Arg253, Gly258, Asp47, and Ala263 (Fig. 4c) and two non-classical hydrogen bonds with Lys119 and Gly182. Suramin also formed the following π-interactions: a π–cation with Arg23, a π–sigma with Thr262, two π–π interactions with Phe181, and two π–alkyl interactions with Ala216 and Tye45. BE value of suramin in the active site of PTP1B was −7.07 kcal mol^{-1}.

2D-interaction mode of the most potent compound **8l** was shown in Fig. 4d, as can be seen in this figure, compound **8l** established six conventional hydrogen bonds with Cys214, Arg220, Arg253 (two interactions), Gln265, and Gln261 and a non-classical hydrogen bond with Gly219. This compound also formed π–π interactions Met257 (π–sulfur), Phe181 (π–π), Tyr45 (π–π), Val48 (a π–sigma and a π–alkyl), Ile218 (π–sigma), and Ala216 (π–alkyl). The BE value of compound **8l** in the active site of PTP1B was −11.72 kcal mol^{-1}.

The comparative analysis of binding energies highlights compound **8l** as the most potent binder, with a BE value lower than those of the native ligand **024** and the reference inhibitor suramin, indicating its enhanced inhibitory efficacy.

As can be seen in Table 1, the second and third most potent compounds against PTP1B were compounds **8h** and **8f**,

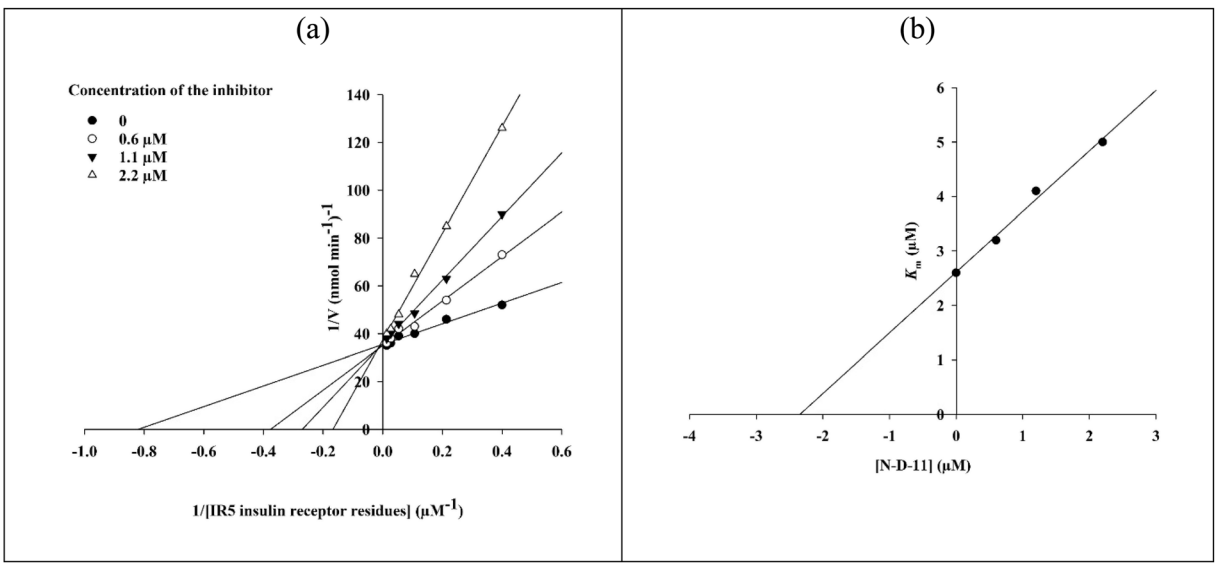

Fig. 3 Kinetic analysis of PTP1B inhibition by compound **8l**. (a) Lineweaver–Burk plots at various inhibitor concentrations (0, 0.6, 1.1, and 2.2 μM). (b) Determination of the inhibition constant (K_i) from the secondary plot of slope *vs.* inhibitor concentration.

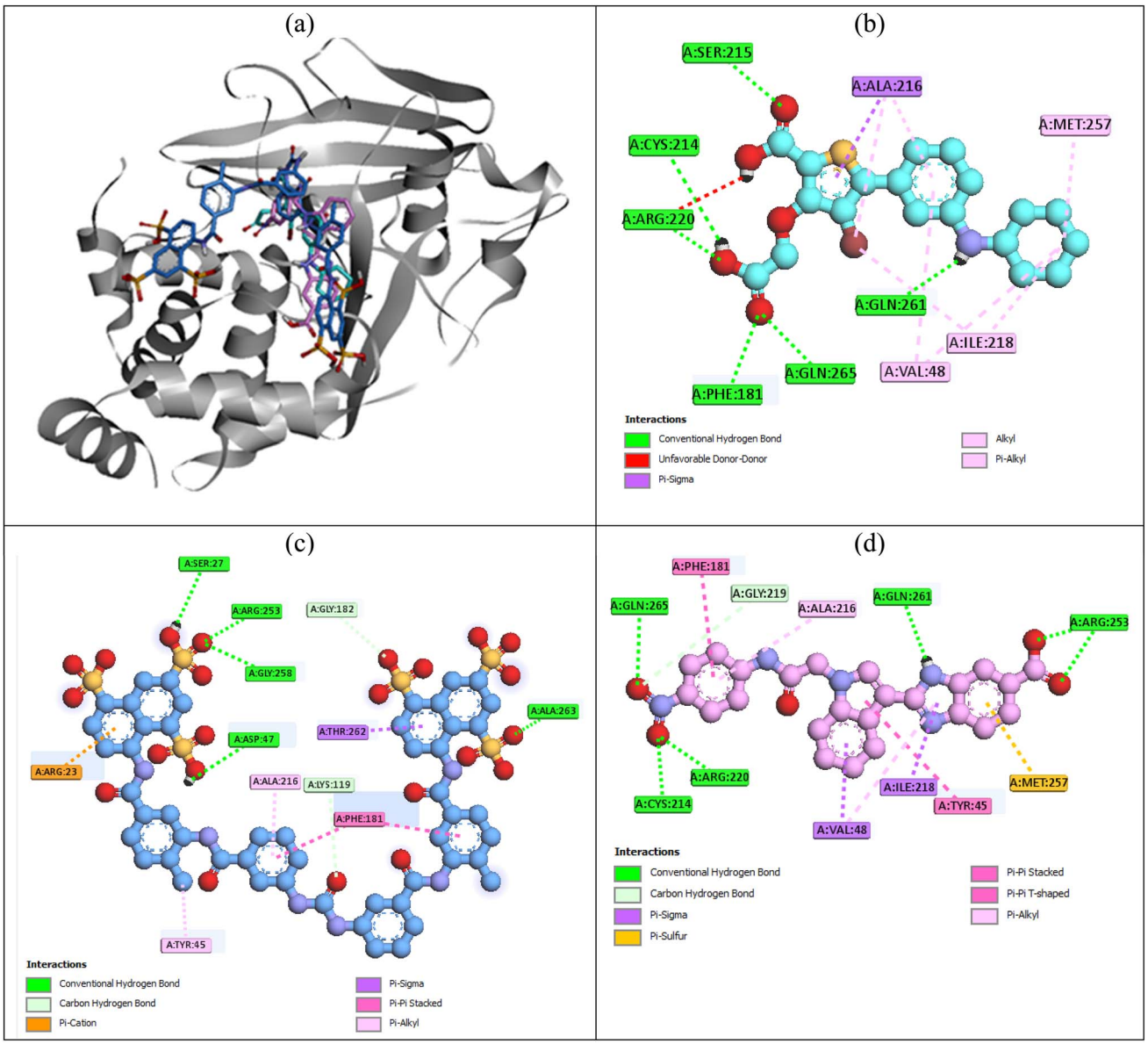

Fig. 4 (a) Superimposed conformer of compounds **024** (cyan), suramin (blue), and **8l** (pink). Interaction modes of compounds **024** (b), suramin (c), and **8l** (d) in the PTP1B's active site.

respectively. The interaction modes of these compounds are shown in Fig. 5. Compound **8h** formed six hydrogen bonds with residues Cys214, Asp47, Arg220, Arg46, Gln265, and Phe181. This compound established the following π interactions with the PTP1B active site: three π–π interactions with Phe181 (two interaction) and Tyr45, three π–alkyl interactions with Val48 (two interaction) and Ala216, a π–cation interaction with Arg46, and a π–sigma with Ala216. The BE of this compound was −9.92 kcal mol^{-1}. Compound **8f** formed five conventional hydrogen bonds Glu114, Ser215, Arg220, Arg23, and Gln261 and a non-classical hydrogen bond with Arg23. This compound also formed one π–sigma with Ala216 and two π–π interactions with Phe181. Four hydrophobic interaction were also observed between compound **8f** and residues Ile218 (two interactions), Met257, and Ala216. The BE value of this compound was −9.6 kcal mol^{-1}.

Computational and experimental data were in strong concordance, as the BE rankings (suramin > **8f** > **8h** > **8l**) predicted by the docking study directly correlated with the potency order observed in the *in vitro* assays (**8l** > **8h** > **8f** > suramin).

Molecular dynamics

The interaction between a substrate and the active site of an enzyme is a highly dynamic process, typically occurring within nanoseconds. To gain meaningful insights into the conformational stability and adaptability of receptor–ligand complexes, it is essential to investigate their behavior in a biologically realistic context that includes explicit water molecules and ions. In this study, molecular dynamics (MD) simulations were employed using the docking structures of suramin (a well-known reference inhibitor), compound **024** (the ligand

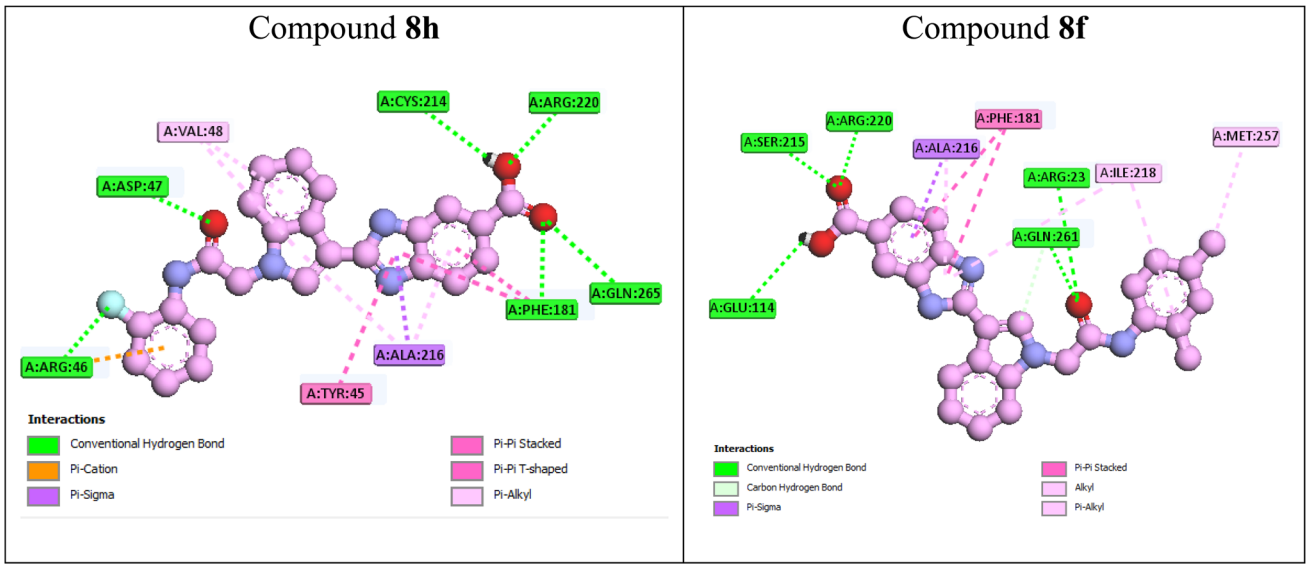

Fig. 5 Interaction modes of compounds **8h** and **8f** in the active site of PTP1B.

observed in the co-crystal structure), and compound **8l** (the most effective PTP1B inhibitor identified *in vitro*). These simulations, conducted in a fully solvated environment, aimed to assess the stability, conformational flexibility, and molecular interactions between the target protein and the selected ligands over the course of the simulation.

In this study, a two-stage MD simulation approach was implemented to evaluate the stability of various ligands bound to the active site of PTP1B. In the first stage, each ligand–enzyme complex underwent a 10 nanoseconds simulation, which demonstrated that the ligands retained stable associations within the binding pocket. To gain deeper insight into their dynamic properties, the simulations were prolonged by an additional 10 nanoseconds. Throughout this extended phase, suramin, **024**, and **8l** consistently exhibited conformational stability within the active site. The resulting trajectory data were then thoroughly analyzed to elucidate the molecular interactions and structural dynamics characterizing each ligand–enzyme complex.

To evaluate the conformational stability of the protein–ligand complexes, root-mean-square deviation (RMSD) and radius of gyration (R_g) analyses were systematically conducted across all simulation trajectories. These parameters were monitored over time, and corresponding plots were generated to visualize structural deviations and variations in molecular compactness throughout the simulation period. Furthermore, root-mean-square fluctuation (RMSF) analysis was carried out on the backbone atoms of PTP1B to assess residue-level flexibility. Together, these evaluations provided valuable insights into the structural integrity of the enzyme and the dynamic behavior of the ligands within the active site, emphasizing the nature of their interactions and the adaptability of the complexes under simulated physiological conditions.

Fig. 6 presents the results of the RMSD analysis, demonstrating the structural stability of the PTP1B–ligand complexes throughout the simulation period. The backbone RMSD values of PTP1B in complex with suramin, **024**, and **8l** exhibited only minor fluctuations, consistently remaining below 0.25 Å, indicative of the enzyme's preserved structural integrity. The mean RMSD values for PTP1B were calculated to be 1.36 Å in the suramin complex and 1.11 Å in the **024** complex, while the value for the **8l** complex was 1.51 Å. The ligands also maintained stable binding conformations, with RMSD values below 0.25 Å during the entire simulation. Specifically, the average RMSD values recorded were 1.45 Å for suramin, 0.87 Å for **024**, and 1.20 for **8l**. These results collectively support the conclusion that both the enzyme and ligands retained significant structural stability under the simulated conditions.

Protein stability during MD simulations is often assessed by examining structural compactness, typically measured by the radius of gyration (R_g). In the case of PTP1B, R_g values were computed throughout the simulation trajectory to evaluate changes in the protein's compactness, as depicted in Fig. 6. The average R_g for the suramin-bound complex was 19.10 Å, whereas the corresponding values for the **024** and **8l** complexes were 19.07 Å and 19.19 Å, respectively. Across all simulations, the R_g values exhibited minimal variation, fluctuating within a narrow range of 18.73 to 19.41 Å. This consistency suggests that PTP1B retained a stable and compact structure throughout the simulation period, reflecting its conformational integrity under the modeled conditions.

The structural and dynamic evaluation of PTP1B offers valuable insight into the enzyme's flexibility and ligand-binding properties (Fig. 7). PTP1B is a single-domain protein characterized by a clearly defined catalytic core, which consists of a central β-sheet flanked by α-helices and flexible loop regions. The catalytic cleft, which functions as the primary ligand-binding site, is located between critical structural elements, notably the WPD loop and the P-loop, both essential for enzymatic function. The WPD loop, encompassing residues 177 to 183 and including the catalytically significant Asp180, plays a central role in modulating enzymatic activity. Meanwhile, the P-loop, which facilitates phosphate binding, includes key

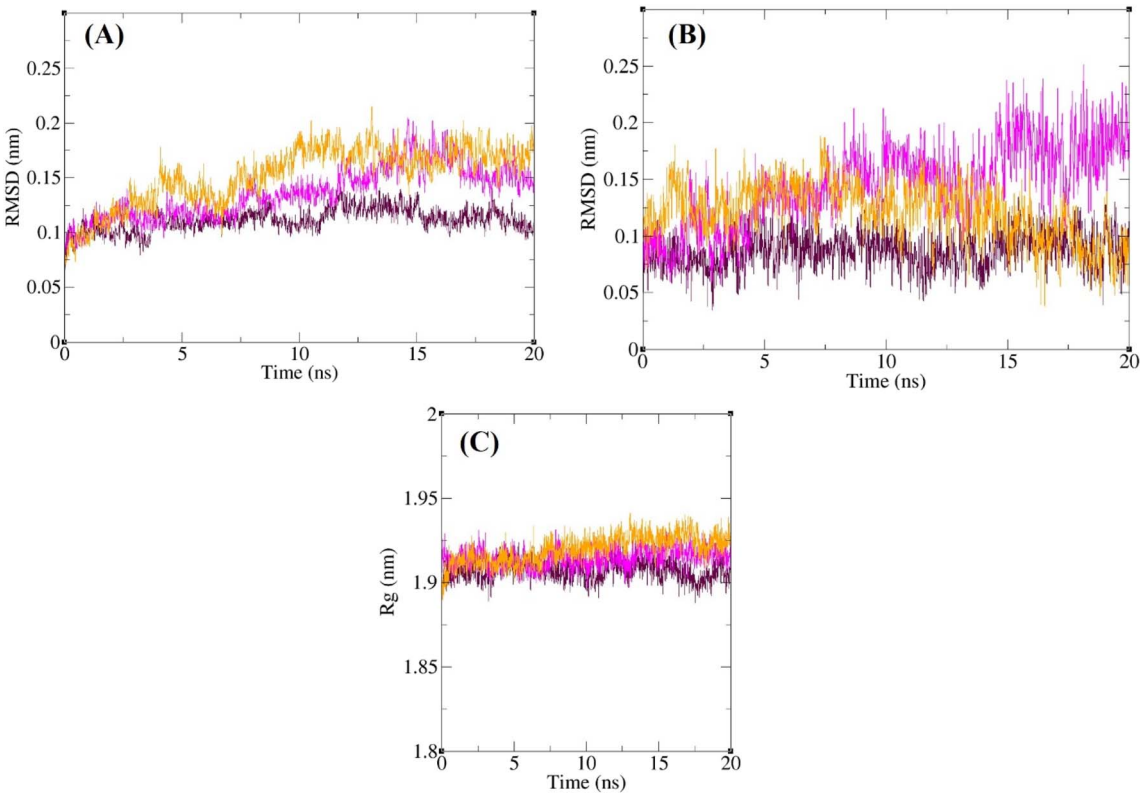

Fig. 6 Superimposed RMSD of Cα atoms of PTP1B in complex with suramin (magenta), **024** (maroon) and **8l** (orange) (A). Superimposed RMSD of suramin (magenta), **024** (maroon) and **8l** (orange) in complex with PTP1B (B). Time dependence of the radius of gyration (R_g) graph of PTP1B in complex with suramin (magenta), **024** (maroon) and **8l** (orange) (C).

residues such as Arg46, Lys119, Ser117, and those within positions 44 to 49. Ligands like compound **024** occupy this cleft, forming stabilizing interactions with conserved amino acids and inducing localized structural adjustments. Peaks observed in the RMSF analysis align with flexible segments near the active site, particularly the WPD and P-loops. These regions display moderate mobility, consistent with their functional roles in ligand accommodation and catalysis. The similarity in RMSF profiles across all three ligand-bound systems suggests that the observed dynamic behavior is driven by their common binding location rather than ligand-specific effects. This finding underscores the structural resilience and functional adaptability of the PTP1B catalytic site in interacting with structurally diverse ligands.

In silico ADMET profiling and evaluation of drug-likeness

In this section, we employed the online pkCSM platform to perform a comprehensive *in silico* prediction of the absorption, distribution, metabolism, excretion, and toxicity (ADMET) properties of our most potent newly synthesized PTP1B inhibitor, compound **8l**, in direct comparison with suramin (Table 3).

The predicted absorption profile of compound **8l** suggests potential improvements over suramin. Both compounds are predicted to have identical, moderately low water solubility (-2.892 log mol L^{-1}), which could pose formulation challenges. A notable predicted advantage for compound **8l** is its markedly higher Caco-2 permeability (-1.013 log P_{app} *vs.* -3.531 for suramin), indicating a greater potential for oral absorption. This is aligned with the predicted human intestinal absorption, where compound **8l** is forecasted to be 73.764% absorbed, compared to 0% for suramin. This difference suggests that compound **8l** might have better oral bioavailability compared to suramin, which is known to be poorly absorbed orally and administered intravenously in the clinic. It should be noted that compound **8l** is predicted to be a potential substrate for P-glycoprotein (P-gp), which could actively efflux it from cells, potentially counteracting its high permeability. Furthermore, compound **8l** is identified as a potential P-gp II inhibitor, indicating a possible risk of drug–drug interactions (DDIs) with co-administered P-gp substrates.

The predicted volume of distribution (VDss) for compound **8l** (0.006 log L kg^{-1}) is slightly higher than that of suramin (-0.017 log L kg^{-1}), which could suggest a somewhat broader tissue distribution for the new compound. The fraction unbound (F_u) in plasma is nearly identical (~0.38), implying a similar extent of plasma protein binding for both. A particularly promising prediction is the significantly enhanced Blood–Brain Barrier (BBB) permeability of compound **8l** (-1.185 log BB) compared to suramin (-3.905 log BB). However, it is important to highlight that BBB permeability predictions from models like pkCSM are statistical and do not equate to established CNS bioavailability. Similarly, the predicted CNS permeability (log PS) of compound **8l** (-2.309) is substantially higher than that of suramin (-5.037).

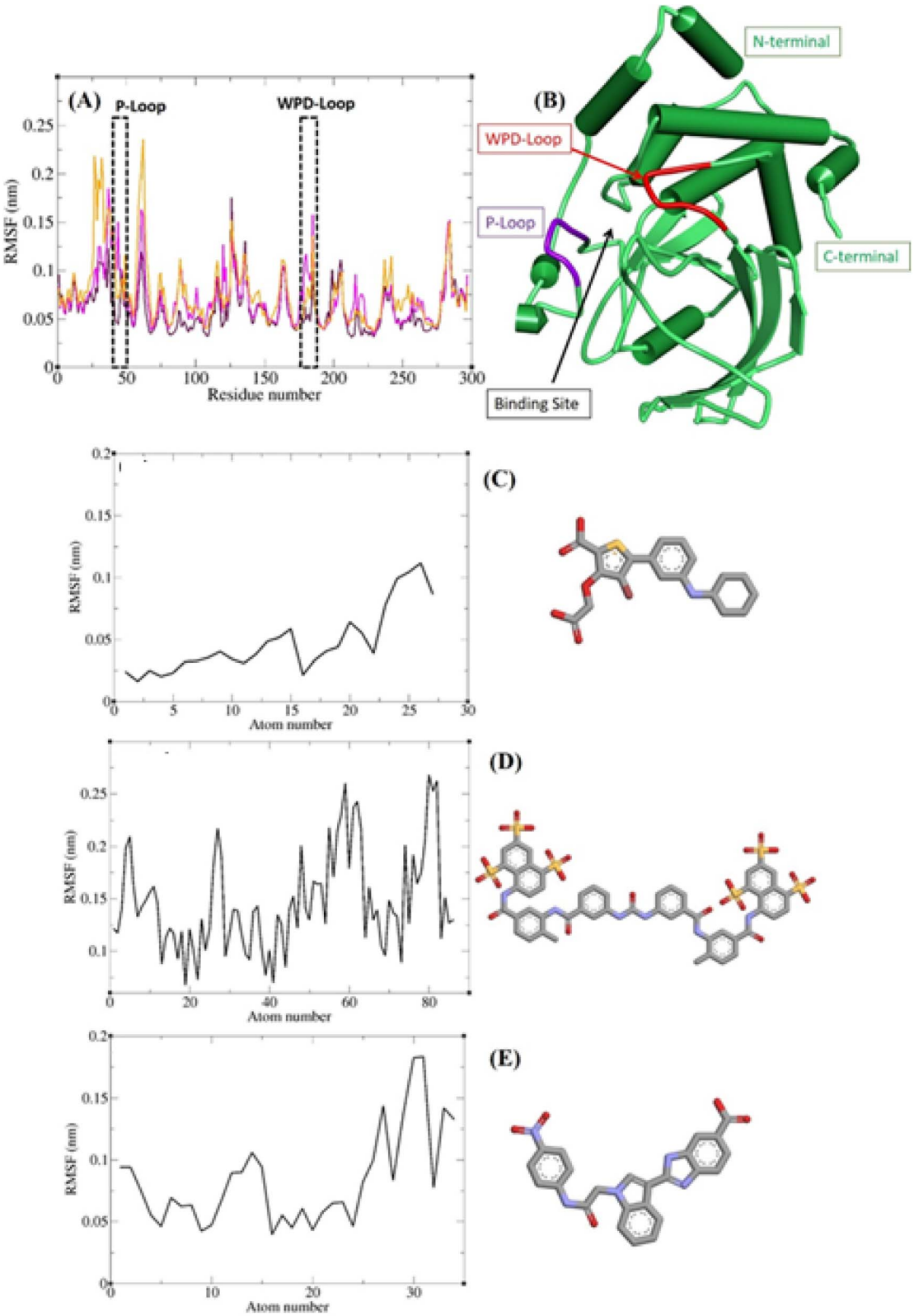

Fig. 7 RMSF graph of the Cα atoms of PTP1B in complex with suramin (magenta), **024** (maroon) and **8l** (orange) (A). The structure of the protein PTP1B, in which the binding site and the main loops are identified (B). RMSF graph of the heavy atoms of **024** (C), suramin (D) and **8l** (E) in complex with PTP1B.

Table 3 Prediction of the pharmacokinetics of compound **8l** as the most potent compound against PTP1B and suramin as the standard drug

Property	Model name	Suramin	**8l**	Unit
Absorption	Water solubility	−2.892	−2.892	Numeric (log mol L^{-1})
	Caco2 permeability	−3.531	−1.013	Numeric (log P_{app} in 10^{-6} cm s^{-1})
	Intestinal absorption (human)	0	73.764	Numeric (% absorbed)
	Skin permeability	−2.735	−2.735	Numeric (log K_p)
	P-glycoprotein substrate	No	Yes	Categorical (yes/no)
	P-glycoprotein I inhibitor	No	No	Categorical (yes/no)
	P-glycoprotein II inhibitor	No	Yes	Categorical (yes/no)
Distribution	VDss (human)	−0.017	0.006	Numeric (log L kg^{-1})
	Fraction unbound (human)	0.378	0.382	Numeric (F_u)
	BBB permeability	−3.905	−1.185	Numeric (log BB)
	CNS permeability	−5.037	−2.309	Numeric (log PS)
Metabolism	CYP2D6 substrate	No	No	Categorical (yes/no)
	CYP3A4 substrate	No	No	Categorical (yes/no)
	CYP1A2 inhibitor	No	Yes	Categorical (yes/no)
	CYP2C19 inhibitor	No	No	Categorical (yes/no)
	CYP2C9 inhibitor	No	Yes	Categorical (yes/no)
	CYP2D6 inhibitor	No	No	Categorical (yes/no)
	CYP3A4 inhibitor	No	No	Categorical (yes/no)
Excretion	Total clearance	−4.274	0.538	Numeric (log mL min^{-1} kg^{-1})
	Renal OCT2 substrate	No	No	Categorical (yes/no)
Toxicity	AMES toxicity	No	No	Categorical (yes/no)
	Max. tolerated dose (human)	0.438	0.439	Numeric (log mg per kg per day)
	hERG I inhibitor	No	No	Categorical (yes/no)
	hERG II inhibitor	Yes	No	Categorical (yes/no)
	Oral rat acute toxicity (LD_{50})	2.482	2.482	Numeric (mol kg^{-1})
	Oral rat chronic toxicity (LOAEL)	7.327	3.123	Numeric (log mg per kg_bw per day)
	Hepatotoxicity	No	Yes	Categorical (yes/no)
	Skin sensitisation	No	No	Categorical (yes/no)
	T. pyriformis toxicity	0.285	0.285	Numeric (log μg L^{-1})
	Minnow toxicity	5.545	1.114	Numeric (log mM)

In terms of metabolism, both compound **8l** and suramin are predicted not to be substrates for the major cytochrome P450 enzymes CYP2D6 and CYP3A4, which could reduce the likelihood of metabolism-mediated DDIs for both compounds. However, a key metabolic difference lies in the predicted inhibition profile. Compound **8l** is predicted to potentially inhibit CYP1A2 and CYP2C9, while suramin is not.

The predicted total clearance of compound **8l** (0.538 log mL min^{-1} kg^{-1}) is significantly higher than that of suramin (−4.274 log mL min^{-1} kg^{-1}), indicating a potentially faster elimination rate for the new compound. Neither compound is

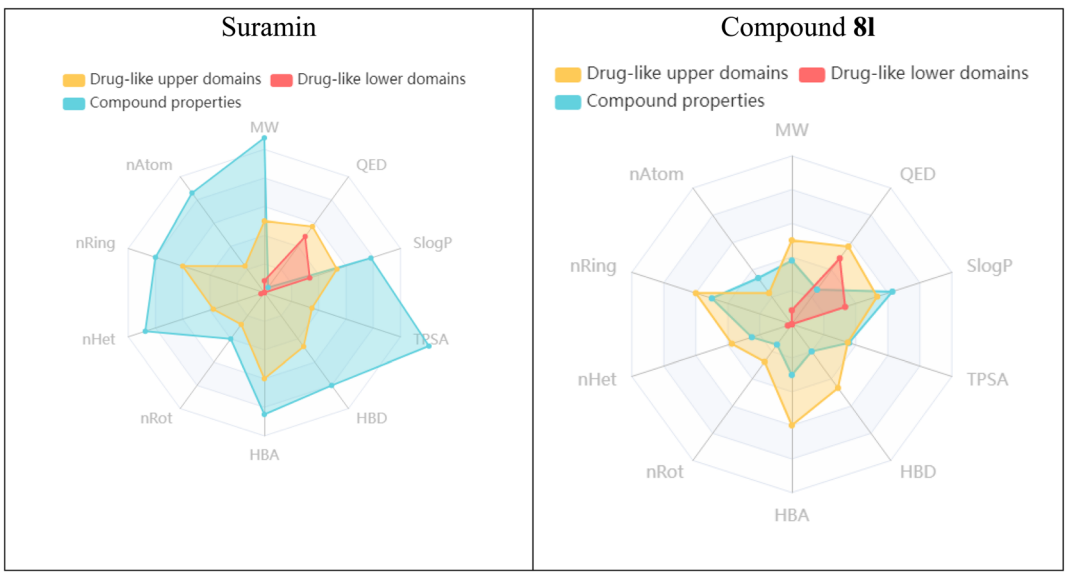

Fig. 8 The predicted ADMET profiles of compound **13j** and acarbose using the admetSAR server.

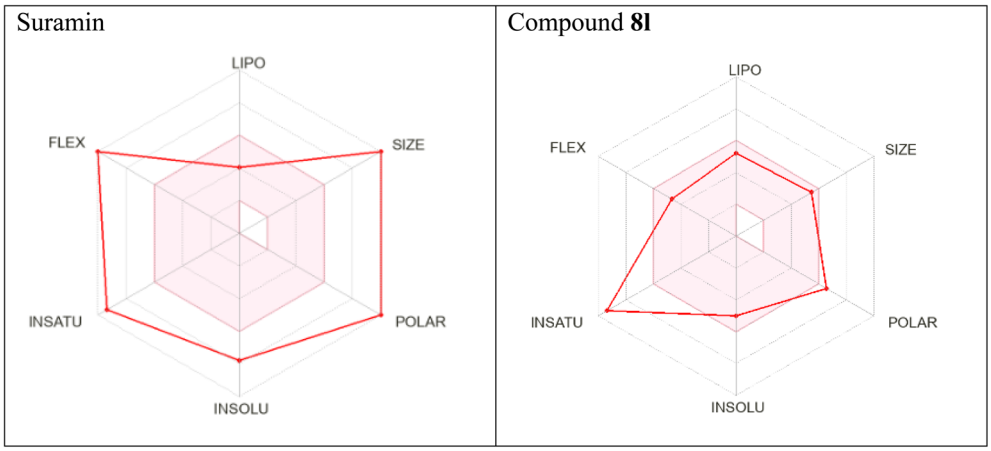

Fig. 9 Bioavailability radars of compounds 8l and suramin.

predicted to be a substrate for the renal organic cation transporter 2 (OCT2), minimizing potential concerns for specific renal transporter-mediated interactions or accumulations.

The toxicity predictions present a mixed profile for compound **8l**. On the positive side, compound **8l** is predicted to be negative for AMES toxicity and skin sensitization, similar to suramin. Notably, compound **8l** is not predicted to be an inhibitor of the hERG II channel, whereas suramin is a predicted hERG II inhibitor. This suggests that compound **8l** may carry a lower potential risk of cardiotoxicity (QT interval prolongation) compared to suramin. However, a significant concern is the prediction of hepatotoxicity for compound **8l**, which was not flagged for suramin. This potential liability requires further experimental validation in subsequent *in vitro* and *in vivo* studies. The predicted chronic toxicity potential, as indicated by the Lower Oral Rat Chronic Toxicity (LOAEL) value for compound **8l** (3.123 log mg per kg_bw per day) compared to suramin (7.327 log mg per kg_bw per day), also warrants careful long-term toxicity assessment. The predicted reduced minnow toxicity value for compound **8l** (1.114 log mM) compared to suramin (5.545 log mM) indicates a potentially lower environmental aquatic toxicity.

Drug-likeness study on compound **8l** and suramin was performed by admetSAR online software. The obtained data were illustrated in Fig. 8. As can be seen in this figure, compound **8l**, shows a higher presence within the drug-likeness acceptable region compared to suramin.

The bioavailability radar plots of suramin and compound **8l** are shown in Fig. 9. The radar plot for compound **8l** appears more balanced and lies predominantly within the desirable range (pink area), whereas the plot for suramin shows significant deviations outside the ideal zone. This graphical analysis confirms that compound **8l** possesses a more favorable drug-like profile compared to suramin.

Conclusion

In conclusion, a novel series of acetamide–indole–benzo[*d*]imidazole–carboxylic acid hybrids (**8a–n**) was successfully designed and synthesized as potential dual-target inhibitors of PTP1B and α-glucosidase. While the majority of compounds exhibited promising PTP1B inhibitory activity, with six derivatives outperforming the standard inhibitor suramin, only two compounds showed marginally improved α-glucosidase inhibition compared to acarbose. Compound **8l** emerged as the most potent PTP1B inhibitor, acting through a competitive mechanism, as confirmed by kinetic analysis. Molecular docking and dynamics simulations supported its stable binding within the PTP1B active site, aligning well with the *in vitro* results. Although the dual inhibitory profile was only partially achieved, the series represents a significant step toward the development of novel PTP1B-targeted therapeutics. Further structural optimization based on the acetamide–indole–benzo[*d*]imidazole scaffold may yield improved dual-target agents for the management of diabetes and related metabolic disorders.

Author contributions

MM and MM-K conceived, designed, and supervised this study. ND, SNG, MM (Marjan Mollazadeh), SH, and NMS synthesized and interpreted analytical data of compounds. *In vitro* experiments were performed by SM, MAF, and BL. *In silico* studies were performed and written by MH and MA. The manuscript was drafted by MM-K. MM reviewed and edited the drafts.

Conflicts of interest

The authors declare no conflict of interest.

Data availability

The data supporting this article have been included as part of the Supplementary information (SI). Supplementary information is available. See DOI: https://doi.org/10.1039/d5ra07935g.

Acknowledgements

This research work was financially supported by the National Institute for Medical Research Development (NIMAD; Grant Number: 4000259).

References

1 A. Artasensi, A. Pedretti, G. Vistoli and L. Fumagalli, *Molecules*, 2020, **25**, 1987.
2 Y. Kong, H. Yang, R. Nie, X. Zhang, H. Zhang and X. Nian, *Eur. J. Med. Res.*, 2025, **30**, 477.
3 M. Genovese, I. Nesi, A. Caselli and P. Paoli, *Molecules*, 2021, **26**, 4818.
4 M. Teimouri, H. Hosseini, Z. ArabSadeghabadi, R. Babaei-Khorzoughi, S. Gorgani-Firuzjaee and R. Meshkani, *J. Physiol. Biochem.*, 2022, **78**, 307–322.
5 E. Di Stefano, T. Oliviero and C. C. Udenigwe, *Curr. Opin. Food Sci.*, 2018, **20**, 7–12.
6 S. Rocha, I. Santos, M. L. Corvo, E. Fernandes and M. Freitas, *Food Funct.*, 2025, **16**, 5231–5277.
7 B. Göke, C. Herrmann, R. Göke, H. C. Fehmann, P. Berghöfer, G. Richter and R. Arnold, *Eur. J. Clin. Invest.*, 1994, **24**, 25–30.
8 X. H. Makhoba, C. Viegas, R. A. Mosa, F. P. Viegas and O. J. Pooe, *Drug Des., Dev. Ther.*, 2020, **14**, 3235–3249.
9 F. F. Lillich, J. D. Imig and E. Proschak, *Front. Pharmacol.*, 2021, **11**, 554961.
10 P. de Sena Murteira Pinheiro, L. S. Franco, T. L. Montagnoli and C. A. M. Fraga, *Expert Opin. Drug Discovery*, 2024, **19**, 451–470.
11 M. I. Campos-Almazan, M. Flores-Ramos, A. Hernández-Campos, R. Castillo, E. Sierra-Campos, K. Torgeson, W. Peti, M. Valdez-Solana, J. Oria-Hernández, S. T. Mendez and A. Castillo-Villanueva, *Bioorg. Med. Chem.*, 2021, **48**, 116418.
12 J. Liu, Y. Chen, J. Y. Li, C. Luo, J. Li, K. X. Chen, X. W. Li and Y. W. Guo, *Mar. Drugs*, 2018, **16**, 97.
13 N. Asemanipoor, M. Mohammadi-Khanaposhtani, S. Moradi, M. Vahidi, M. Asadi, M. A. Faramarzi, M. Mahdavi, M. Biglar, B. Larijani, H. Hamedifar and M. H. Hajimiri, *Bioorg. Chem.*, 2020, **95**, 103482.
14 M. H. Sayahi, S. Zareei, M. Halimi, M. Alikhani, A. Moazzam, M. Mohammadi-Khanaposhtani, S. Mojtabavi, M. A. Faramarzi, H. Rastegar, P. Taslimi and E. H. Ibrahim, *Sci. Rep.*, 2024, **14**, 15791.
15 A. M. Taherkhani, M. H. Sayahi, B. Hassani, N. Dastyafteh, M. Mohammadi-Khanaposhtani, E. Rafiei, M. Meshkani, S. Safapoor, M. M. Tehrani, B. Larijani and M. Mahdavi, *J. Mol. Struct.*, 2025, **1336**, 142089.
16 A. S. Shokouhi Asl, M. H. Sayahi, M. H. Hashempur, C. Irajie, A. H. Alaeddini, S. N. Ghafouri, M. Noori, N. Dastyafteh, J. Mottaghipisheh, M. Asadi and B. Larijani, *Sci. Rep.*, 2025, **15**, 655.
17 M. K. Ghomi, N. Dastyafteh, M. N. Montazer, M. Noori, S. Mojtabavi, M. A. Faramarzi, S. M. Hashemi and M. Mahdavi, *Sci. Rep.*, 2023, **13**, 501.
18 N. Dastyafteh, M. Negahdaripour, M. H. Sayahi, M. Emami, Y. Ghasemi, E. Safaei, H. Azizian, Z. P. Jahromi, M. Asadi, M. R. Mohajeri-Tehrani and F. Zare, *RSC Adv.*, 2024, **14**, 35323–35335.
19 W. S. Liu, R. R. Wang, H. Yue, Z. H. Zheng, X. H. Lu, S. Q. Wang, W. L. Dong and R. L. Wang, *J. Biomol. Struct. Dyn.*, 2020, **38**, 3814–3824.
20 M. J. Abraham, T. Murtola, R. Schulz, S. Páll, J. C. Smith, B. Hess and E. Lindahl, *SoftwareX*, 2015, **1**, 19–25.
21 V. Zoete, M. A. Cuendet, A. Grosdidier and O. Michielin, *J. Comput. Chem.*, 2011, **32**, 2359–2368.
22 D. E. Pires, T. L. Blundell and D. B. Ascher, *J. Med. Chem.*, 2015, **58**, 4066–4072.
23 H. Yang, C. Lou, L. Sun, J. Li, Y. Cai, Z. Wang, W. Li, G. Liu and Y. Tang, *Bioinformatics*, 2019, **35**, 1067–1069.
24 A. Daina, O. Michielin and V. Zoete, *Sci. Rep.*, 2017, **7**, 42717.